J/ψ and $\psi(2S)$ production at forward rapidity in p+p collisions at $\sqrt{s} = 510$ GeV

U.A. Acharya,[20] A. Adare,[11] C. Aidala,[43] N.N. Ajitanand,[62,*] Y. Akiba,[57,58,†] R. Akimoto,[10] M. Alfred,[23] N. Apadula,[28,63] Y. Aramaki,[57] H. Asano,[35,57] E.T. Atomssa,[63] T.C. Awes,[52] B. Azmoun,[7] V. Babintsev,[24] M. Bai,[6] N.S. Bandara,[42] B. Bannier,[63] K.N. Barish,[8] S. Bathe,[5,58] A. Bazilevsky,[7] M. Beaumier,[8] S. Beckman,[11] R. Belmont,[11,43,50] A. Berdnikov,[60] Y. Berdnikov,[60] D. Black,[8] J.S. Bok,[49] K. Boyle,[58] M.L. Brooks,[38] J. Bryslawskyj,[5,8] H. Buesching,[7] V. Bumazhnov,[24] S. Campbell,[12,28] V. Canoa Roman,[63] C.-H. Chen,[58] C.Y. Chi,[12] M. Chiu,[7] I.J. Choi,[25] J.B. Choi,[30,*] T. Chujo,[66] Z. Citron,[68] M. Connors,[20,58] M. Csanád,[15] T. Csörgő,[16,69] T.W. Danley,[51] A. Datta,[48] M.S. Daugherity,[1] G. David,[7,14,63] K. DeBlasio,[48] K. Dehmelt,[63] A. Denisov,[24] A. Deshpande,[7,58,63] E.J. Desmond,[7] L. Ding,[28] A. Dion,[63] J.H. Do,[70] A. Drees,[63] K.A. Drees,[6] J.M. Durham,[38] A. Durum,[24] A. Enokizono,[57,59] H. En'yo,[57] R. Esha,[63] S. Esumi,[66] B. Fadem,[44] W. Fan,[63] N. Feege,[63] D.E. Fields,[48] M. Finger,[9] M. Finger, Jr.,[9] D. Fitzgerald,[43] S.L. Fokin,[34] J.E. Frantz,[51] A. Franz,[7] A.D. Frawley,[19] C. Gal,[63] P. Gallus,[13] E.A. Gamez,[43] P. Garg,[3,63] H. Ge,[63] F. Giordano,[25] A. Glenn,[37] Y. Goto,[57,58] N. Grau,[2] S.V. Greene,[67] M. Grosse Perdekamp,[25] Y. Gu,[62] T. Gunji,[10] H. Guragain,[20] T. Hachiya,[46,57,58] J.S. Haggerty,[7] K.I. Hahn,[17] H. Hamagaki,[10] S.Y. Han,[17,33,57] J. Hanks,[63] S. Hasegawa,[29] T.O.S. Haseler,[20] X. He,[20] T.K. Hemmick,[63] J.C. Hill,[28] K. Hill,[11] A. Hodges,[20] R.S. Hollis,[8] K. Homma,[22] B. Hong,[33] T. Hoshino,[22] J. Huang,[7,38] S. Huang,[67] Y. Ikeda,[57] K. Imai,[29] Y. Imazu,[57] M. Inaba,[66] A. Iordanova,[8] D. Isenhower,[1] S. Ishimaru,[46] D. Ivanishchev,[55] B.V. Jacak,[63] S.J. Jeon,[45] M. Jezghani,[20] Z. Ji,[63] J. Jia,[7,62] X. Jiang,[38] B.M. Johnson,[7,20] E. Joo,[33] K.S. Joo,[45] D. Jouan,[53] D.S. Jumper,[25] J.H. Kang,[70] J.S. Kang,[21] D. Kawall,[42] A.V. Kazantsev,[34] J.A. Key,[48] V. Khachatryan,[63] A. Khanzadeev,[55] A. Khatiwada,[38] K. Kihara,[66] C. Kim,[33] D.H. Kim,[17] D.J. Kim,[31] E.-J. Kim,[30] H.-J. Kim,[70] M. Kim,[57,61] Y.K. Kim,[21] D. Kincses,[15] E. Kistenev,[7] J. Klatsky,[19] D. Kleinjan,[8] P. Kline,[63] T. Koblesky,[11] M. Kofarago,[15,69] J. Koster,[58] D. Kotov,[55,60] B. Kurgyis,[15] K. Kurita,[59] M. Kurosawa,[57,58] Y. Kwon,[70] R. Lacey,[62] J.G. Lajoie,[28] A. Lebedev,[28] K.B. Lee,[38] S.H. Lee,[28,63] M.J. Leitch,[38] M. Leitgab,[25] Y.H. Leung,[63] N.A. Lewis,[43] X. Li,[38] S.H. Lim,[11,38,56,70] M.X. Liu,[38] S. Lökös,[15,16] D. Lynch,[7] T. Majoros,[14] Y.I. Makdisi,[6] M. Makek,[68,71] A. Manion,[63] V.I. Manko,[34] E. Mannel,[7] M. McCumber,[38] P.L. McGaughey,[38] D. McGlinchey,[11,38] C. McKinney,[25] A. Meles,[49] M. Mendoza,[8] B. Meredith,[12] W.J. Metzger,[16] Y. Miake,[66] A.C. Mignerey,[41] A.J. Miller,[1] A. Milov,[68] D.K. Mishra,[4] J.T. Mitchell,[7] Iu. Mitrankov,[60] G. Mitsuka,[32,57] S. Miyasaka,[57,65] S. Mizuno,[57,66] P. Montuenga,[25] T. Moon,[33,70] D.P. Morrison,[7] S.I. Morrow,[67] T.V. Moukhanova,[34] B. Mulilo,[33,57] T. Murakami,[35,57] J. Murata,[57,59] A. Mwai,[62] S. Nagamiya,[32,57] K. Nagashima,[22,57] J.L. Nagle,[11] M.I. Nagy,[15] I. Nakagawa,[57,58] H. Nakagomi,[57,66] K. Nakano,[57,65] C. Nattrass,[64] S. Nelson,[18] P.K. Netrakanti,[4] M. Nihashi,[22,57] T. Niida,[66] R. Nishitani,[46] R. Nouicer,[7,58] T. Novák,[16,69] N. Novitzky,[31,63,66] A.S. Nyanin,[34] E. O'Brien,[7] C.A. Ogilvie,[28] J.D. Orjuela Koop,[11] J.D. Osborn,[43] A. Oskarsson,[39] K. Ozawa,[32,66] R. Pak,[7] V. Pantuev,[26] V. Papavassiliou,[49] S. Park,[57,61,63] S.F. Pate,[49] L. Patel,[20] M. Patel,[28] J.-C. Peng,[25] W. Peng,[67] D.V. Perepelitsa,[7,11,12] G.D.N. Perera,[49] D.Yu. Peressounko,[34] C.E. PerezLara,[63] J. Perry,[28] R. Petti,[7,63] C. Pinkenburg,[7] R. Pinson,[1] R.P. Pisani,[7] A. Pun,[51] M.L. Purschke,[7] P.V. Radzevich,[60] J. Rak,[31] N. Ramasubramanian,[63] I. Ravinovich,[68] K.F. Read,[52,64] D. Reynolds,[62] V. Riabov,[47,55] Y. Riabov,[55,60] D. Richford,[5] T. Rinn,[25,28] N. Riveli,[51] D. Roach,[67] S.D. Rolnick,[8] M. Rosati,[28] Z. Rowan,[5] J.G. Rubin,[43] J. Runchey,[28] N. Saito,[32] T. Sakaguchi,[7] H. Sako,[29] V. Samsonov,[47,55] M. Sarsour,[20] S. Sato,[29] S. Sawada,[32] C.Y. Scarlett,[18] B. Schaefer,[67] B.K. Schmoll,[64] K. Sedgwick,[8] J. Seele,[58] R. Seidl,[57,58] A. Sen,[28,64] R. Seto,[8] P. Sett,[4] A. Sexton,[41] D. Sharma,[63] I. Shein,[24] T.-A. Shibata,[57,65] K. Shigaki,[22] M. Shimomura,[28,46] P. Shukla,[4] A. Sickles,[7,25] C.L. Silva,[38] D. Silvermyr,[39,52] B.K. Singh,[3] C.P. Singh,[3] V. Singh,[3] M. Slunečka,[9] K.L. Smith,[19] R.A. Soltz,[37] W.E. Sondheim,[38] S.P. Sorensen,[64] I.V. Sourikova,[7] P.W. Stankus,[52] M. Stepanov,[42,*] S.P. Stoll,[7] T. Sugitate,[22] A. Sukhanov,[7] T. Sumita,[57] J. Sun,[63] X. Sun,[20] Z. Sun,[14] S. Suzuki,[46] J. Sziklai,[69] A. Takahara,[10] A. Taketani,[57,58] K. Tanida,[29,58,61] M.J. Tannenbaum,[7] S. Tarafdar,[67,68] A. Taranenko,[47,62] R. Tieulent,[40] A. Timilsina,[28] T. Todoroki,[57,58,66] M. Tomášek,[13] H. Torii,[10] M. Towell,[1] R. Towell,[1] R.S. Towell,[1] I. Tserruya,[68] Y. Ueda,[22] B. Ujvari,[14] H.W. van Hecke,[38] M. Vargyas,[15,69] J. Velkovska,[67] M. Virius,[13] V. Vrba,[13,27] E. Vznuzdaev,[55] X.R. Wang,[49,58] Z. Wang,[5] D. Watanabe,[22] Y. Watanabe,[57,58] Y.S. Watanabe,[10,32] F. Wei,[49] S. Whitaker,[28] S. Wolin,[25] C.P. Wong,[20] C.L. Woody,[7] Y. Wu,[8] M. Wysocki,[52] B. Xia,[51] Q. Xu,[67] L. Xue,[20] S. Yalcin,[63] Y.L. Yamaguchi,[10,58,63] A. Yanovich,[24] J.H. Yoo,[33,58] I. Yoon,[61] I. Younus,[36] H. Yu,[49,54] I.E. Yushmanov,[34] W.A. Zajc,[12] A. Zelenski,[6] Y. Zhai,[28] S. Zharko,[60] and L. Zou[8]

(PHENIX Collaboration)

[1] *Abilene Christian University, Abilene, Texas 79699, USA*
[2] *Department of Physics, Augustana University, Sioux Falls, South Dakota 57197, USA*
[3] *Department of Physics, Banaras Hindu University, Varanasi 221005, India*

[4] *Bhabha Atomic Research Centre, Bombay 400 085, India*
[5] *Baruch College, City University of New York, New York, New York, 10010 USA*
[6] *Collider-Accelerator Department, Brookhaven National Laboratory, Upton, New York 11973-5000, USA*
[7] *Physics Department, Brookhaven National Laboratory, Upton, New York 11973-5000, USA*
[8] *University of California-Riverside, Riverside, California 92521, USA*
[9] *Charles University, Ovocný trh 5, Praha 1, 116 36, Prague, Czech Republic*
[10] *Center for Nuclear Study, Graduate School of Science, University of Tokyo, 7-3-1 Hongo, Bunkyo, Tokyo 113-0033, Japan*
[11] *University of Colorado, Boulder, Colorado 80309, USA*
[12] *Columbia University, New York, New York 10027 and Nevis Laboratories, Irvington, New York 10533, USA*
[13] *Czech Technical University, Zikova 4, 166 36 Prague 6, Czech Republic*
[14] *Debrecen University, H-4010 Debrecen, Egyetem tér 1, Hungary*
[15] *ELTE, Eötvös Loránd University, H-1117 Budapest, Pázmány P. s. 1/A, Hungary*
[16] *Eszterházy Károly University, Károly Róbert Campus, H-3200 Gyöngyös, Mátrai út 36, Hungary*
[17] *Ewha Womans University, Seoul 120-750, Korea*
[18] *Florida A&M University, Tallahassee, FL 32307, USA*
[19] *Florida State University, Tallahassee, Florida 32306, USA*
[20] *Georgia State University, Atlanta, Georgia 30303, USA*
[21] *Hanyang University, Seoul 133-792, Korea*
[22] *Hiroshima University, Kagamiyama, Higashi-Hiroshima 739-8526, Japan*
[23] *Department of Physics and Astronomy, Howard University, Washington, DC 20059, USA*
[24] *IHEP Protvino, State Research Center of Russian Federation, Institute for High Energy Physics, Protvino, 142281, Russia*
[25] *University of Illinois at Urbana-Champaign, Urbana, Illinois 61801, USA*
[26] *Institute for Nuclear Research of the Russian Academy of Sciences, prospekt 60-letiya Oktyabrya 7a, Moscow 117312, Russia*
[27] *Institute of Physics, Academy of Sciences of the Czech Republic, Na Slovance 2, 182 21 Prague 8, Czech Republic*
[28] *Iowa State University, Ames, Iowa 50011, USA*
[29] *Advanced Science Research Center, Japan Atomic Energy Agency, 2-4 Shirakata Shirane, Tokai-mura, Naka-gun, Ibaraki-ken 319-1195, Japan*
[30] *Jeonbuk National University, Jeonju, 54896, Korea*
[31] *Helsinki Institute of Physics and University of Jyväskylä, P.O.Box 35, FI-40014 Jyväskylä, Finland*
[32] *KEK, High Energy Accelerator Research Organization, Tsukuba, Ibaraki 305-0801, Japan*
[33] *Korea University, Seoul, 02841*
[34] *National Research Center "Kurchatov Institute", Moscow, 123098 Russia*
[35] *Kyoto University, Kyoto 606-8502, Japan*
[36] *Physics Department, Lahore University of Management Sciences, Lahore 54792, Pakistan*
[37] *Lawrence Livermore National Laboratory, Livermore, California 94550, USA*
[38] *Los Alamos National Laboratory, Los Alamos, New Mexico 87545, USA*
[39] *Department of Physics, Lund University, Box 118, SE-221 00 Lund, Sweden*
[40] *IPNL, CNRS/IN2P3, Univ Lyon, Universit Lyon 1, F-69622, Villeurbanne, France*
[41] *University of Maryland, College Park, Maryland 20742, USA*
[42] *Department of Physics, University of Massachusetts, Amherst, Massachusetts 01003-9337, USA*
[43] *Department of Physics, University of Michigan, Ann Arbor, Michigan 48109-1040, USA*
[44] *Muhlenberg College, Allentown, Pennsylvania 18104-5586, USA*
[45] *Myongji University, Yongin, Kyonggido 449-728, Korea*
[46] *Nara Women's University, Kita-uoya Nishi-machi Nara 630-8506, Japan*
[47] *National Research Nuclear University, MEPhI, Moscow Engineering Physics Institute, Moscow, 115409, Russia*
[48] *University of New Mexico, Albuquerque, New Mexico 87131, USA*
[49] *New Mexico State University, Las Cruces, New Mexico 88003, USA*
[50] *Physics and Astronomy Department, University of North Carolina at Greensboro, Greensboro, North Carolina 27412, USA*
[51] *Department of Physics and Astronomy, Ohio University, Athens, Ohio 45701, USA*
[52] *Oak Ridge National Laboratory, Oak Ridge, Tennessee 37831, USA*
[53] *IPN-Orsay, Univ. Paris-Sud, CNRS/IN2P3, Université Paris-Saclay, BP1, F-91406, Orsay, France*
[54] *Peking University, Beijing 100871, People's Republic of China*
[55] *PNPI, Petersburg Nuclear Physics Institute, Gatchina, Leningrad region, 188300, Russia*
[56] *Pusan National University, Busan, 46241, South Korea*
[57] *RIKEN Nishina Center for Accelerator-Based Science, Wako, Saitama 351-0198, Japan*
[58] *RIKEN BNL Research Center, Brookhaven National Laboratory, Upton, New York 11973-5000, USA*
[59] *Physics Department, Rikkyo University, 3-34-1 Nishi-Ikebukuro, Toshima, Tokyo 171-8501, Japan*
[60] *Saint Petersburg State Polytechnic University, St. Petersburg, 195251 Russia*
[61] *Department of Physics and Astronomy, Seoul National University, Seoul 151-742, Korea*
[62] *Chemistry Department, Stony Brook University, SUNY, Stony Brook, New York 11794-3400, USA*
[63] *Department of Physics and Astronomy, Stony Brook University, SUNY, Stony Brook, New York 11794-3800, USA*
[64] *University of Tennessee, Knoxville, Tennessee 37996, USA*
[65] *Department of Physics, Tokyo Institute of Technology, Oh-okayama, Meguro, Tokyo 152-8551, Japan*
[66] *Tomonaga Center for the History of the Universe, University of Tsukuba, Tsukuba, Ibaraki 305, Japan*

[67] Vanderbilt University, Nashville, Tennessee 37235, USA
[68] Weizmann Institute, Rehovot 76100, Israel
[69] Institute for Particle and Nuclear Physics, Wigner Research Centre for Physics, Hungarian Academy of Sciences (Wigner RCP, RMKI) H-1525 Budapest 114, POBox 49, Budapest, Hungary
[70] Yonsei University, IPAP, Seoul 120-749, Korea
[71] Department of Physics, Faculty of Science, University of Zagreb, Bijenička c. 32 HR-10002 Zagreb, Croatia
(Dated: February 21, 2020)

The PHENIX experiment at the Relativistic Heavy Ion Collider has measured the differential cross section, mean transverse momentum, mean transverse momentum squared of inclusive J/ψ and cross-section ratio of $\psi(2S)$ to J/ψ at forward rapidity in p+p collisions at $\sqrt{s} = 510$ GeV via the dimuon decay channel. Comparison is made to inclusive J/ψ cross sections measured at $\sqrt{s} = 200$ GeV and 2.76–13 TeV. The result is also compared to leading-order nonrelativistic QCD calculations coupled to a color-glass-condensate description of the low-x gluons in the proton at low transverse momentum (p_T) and to next-to-leading order nonrelativistic QCD calculations for the rest of the p_T range. These calculations overestimate the data at low p_T. While consistent with the data within uncertainties above ≈ 3 GeV/c, the calculations are systematically below the data. The total cross section times the branching ratio is BR $d\sigma_{pp}^{J/\psi}/dy(1.2 < |y| < 2.2, 0 < p_T < 10$ GeV/$c) = 54.3 \pm 0.5$ (stat) ± 5.5 (syst) nb.

I. INTRODUCTION

Charmonium states such as J/ψ and $\psi(2S)$ mesons are bound states of a charm and anti-charm quark ($c\bar{c}$). At the Relativistic Heavy Ion Collider (RHIC) energies, they are produced mostly from hard scattering of two gluons into a $c\bar{c}$ pair followed by the evolution of this pair through a hadronization process to form a physical charmonium. Despite several decades of extensive studies [1–9] since the discovery of J/ψ, we still have very limited knowledge about the J/ψ production mechanism and hadronization. Therefore, carrying out as many charmonium measurements as possible in p+p collisions over a wide range of transverse momentum (p_T) and of rapidity (y) at different energies is essential to understanding production mechanisms. These measurements over a wide range of p_T (down to zero p_T) and rapidity allow calculating quantities, such as the mean transverse momentum $\langle p_T \rangle$, the mean transverse momentum squared $\langle p_{\rm T}^2 \rangle$, and the p_T-integrated cross section $d\sigma/dy$. The collision energy dependence of these quantities can put stringent constraints on the different theoretical approaches that are used to describe the hadronic production of J/ψ. These approaches include the color-evaporation model (CEM) [10, 11], the color-singlet model (CSM) [12] and the nonrelativistic quantum chromodynamics formalism (NRQCD) [13]. In this work, we compare the data to NRQCD, an effective field theory derived from QCD and valid for heavy-quark pairs with low relative velocity, where a J/ψ can be formed from $c\bar{c}$ pair produced in a color-singlet or a color-octet state.

In this paper, we present the inclusive J/ψ production cross section and the ratio of $\psi(2S)$ to J/ψ production cross sections at forward rapidity ($1.2 < |y| < 2.2$) measured in p+p collisions at center of mass energy $\sqrt{s} =$ 510 GeV. These mesons are measured in the dimuon decay channel. The J/ψ inclusive differential cross sections are obtained as a function of p_T and y over a wide range of p_T. The J/ψ and $\psi(2S)$ results at $\sqrt{s} = 510$ GeV are the first measurements at this rapidity. Comparisons to similar PHENIX measurements performed at $\sqrt{s} = 200$ GeV [2] and Large Hadron Collider (LHC) measurements at $\sqrt{s} = 2.76$, 5.02, 7, 8 and 13 TeV [3–6] allow studying the variations of $\langle p_T \rangle$, $\langle p_{\rm T}^2 \rangle$ and $d\sigma/dy$ as a function of $\sqrt{s}$. The results are also compared to next-to-leading order (NLO) NRQCD calculations [8].

The paper is organized as follows: the PHENIX apparatus is described in Sec. II, the data samples used for this analysis and the analysis procedure are discussed in Sec. III, while the results are presented and compared to measurements at different $\sqrt{s}$ as well as to models in Sec. IV.

II. EXPERIMENTAL SETUP

A complete description of the PHENIX detector can be found in Ref. [14]. Only the detector systems relevant to this measurement are briefly described here.

The PHENIX muon spectrometers, see Fig. 1, cover the full aziumth and the north (south) arm cover forward (backward) rapidity, $1.2 < y < 2.2$ ($-2.2 < y < -1.2$). Each muon spectrometer comprises a hadronic absorber, a magnet, a muon tracker (MuTr), and a muon identifier (MuID). The absorbers comprise layers of copper, iron and stainless steel and have about 7.2 interaction lengths. Following the absorber in each muon arm is the MuTr, which comprises three stations of cathode strip chambers in a radial magnetic field with an integrated bending power of 0.8 T·m. The MuID comprises five alternating steel absorbers and Iarocci tubes. The composite momentum resolution, $\delta p/p$, of particles in the analyzed momentum range is about 5%, independent of momentum and dominated by multiple scattering. Muon

* Deceased
† PHENIX Spokesperson: akiba@rcf.rhic.bnl.gov

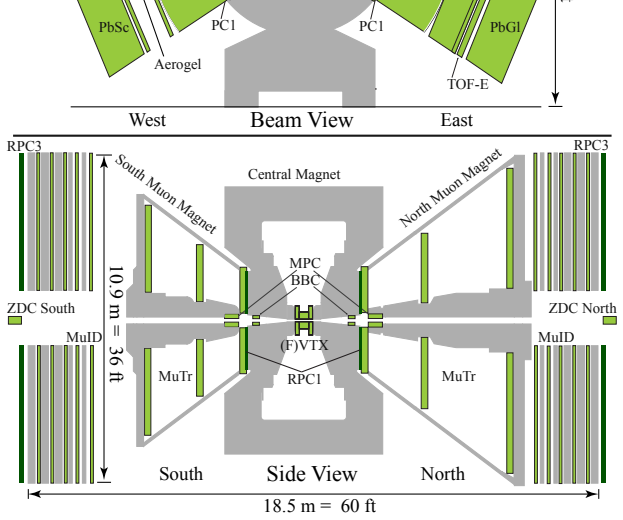

FIG. 1. A side view of the PHENIX detector, concentrating on the muon arm instrumentation.

candidates are identified by reconstructed tracks in the MuTr matched to MuID tracks that penetrate through to the last MuID plane.

Since 2012 the PHENIX detector had a new forward vertex detector (FVTX) [15], which comprises four planes of silicon strip detectors, finely segmented in radius and coarsely segmented in azimuth. For the subset of muon candidate tracks passing several of these detector planes, this additional information was used to improve mass resolution by a factor of 1.5 for studying $\psi(2S)$.

Another detector system relevant to this analysis is the beam-beam counter (BBC), comprising two arrays of 64 Čerenkov counters, located on both sides of the interaction point and covering the pseudorapidity range $3.1 < |\eta| < 3.9$. The BBC system was used to measure the p+p collision vertex position along the beam axis ($z_{\rm vtx}$), with 2 cm resolution, and initial collision time. It was also used to measure the beam luminosity and form a minimum bias (MB) trigger.

III. DATA ANALYSIS

The results presented here are based on the data sample collected by PHENIX during the 2013 p+p run at $\sqrt{s}$ = 510 GeV. The BBC counters provided the MB trigger, which required at least one hit in each of the BBCs. Events, in coincidence with the MB trigger, containing a muon pair within the acceptance of the spectrometer are selected by the level-1 dimuon trigger (MuIDLL1-2D) requiring that at least two tracks penetrate through the MuID to its last layer. The data sample, used in this analysis, corresponds to 3.02×10^{12} MB events or to an integrated luminosity of 94.4 pb^{-1}.

A. Raw yield extraction

A set of quality cuts is applied to the data to select good p+p events and good muon candidates as well as to improve the signal-to-background ratio. Good p+p events are selected by requiring that the collision occurs in the fiducial interaction region $|z_{\rm vtx}| < 30$ cm as measured by the BBC. Each reconstructed muon candidate comprises a combination of reconstructed muon tracks in the MuTr and in the MuID. The MuTr track is required to have more than 9 hits out of the maximum possible of 16 while the MuID track is required to have more than 6 hits out of the maximum possible of 10. In addition, a cut on individual MuTr track χ^2 of 23 is applied. The MuTr track χ^2 is calculated from the difference between the measured hit positions of the track and the subsequent fit for each MuTr track. The MuTr tracks are then matched to the MuID tracks at the first MuID layer by applying cuts on maximum position and angle differences. Furthermore, there is a minimum allowed single muon momentum along the beam axis, p_z, which is reconstructed and energy-loss corrected at the collision vertex, of 3.0 GeV/c corresponding to the momentum cut effectively imposed by the absorbers. Finally, a cut on the χ^2 of the fit of the two muon tracks to the common vertex of the two candidate tracks near the interaction point was applied.

The invariant mass distribution is formed by combining muon candidate tracks of opposite charges (unlike-sign). In addition to the charmonium signal, the resulting unlike-sign dimuon spectrum includes correlated and uncorrelated pairs. In the J/ψ and $\psi(2S)$ region, the correlated pairs arise from correlated semi-muonic decays of charmed hadrons, beauty and the Drell-Yan process as well as light hadron decays. The uncorrelated pairs are mainly coming from the decays of light hadrons ($\pi^{\pm}$, $K^{\pm}$ and K^0) which decay before or after passing through the absorber, and form the combinatorial background.

The combinatorial background is estimated using two methods: The first one derives the combinatorial background from the mass distribution of the same sign (like-sign) pairs of muon candidates within the same event. The second method derives the combinatorial background from the mass distribution of the unlike-sign pairs of muon candidates from different events (mixed-event) of z-vertex position within 2 cm. The normalization of the mass distribution of the combinatorial background from the like-sign dimuon distributions (N_{++} and N_{--}) is calculated as: $N_{\rm CB} = 2\sqrt{N_{++}N_{--}}$. The mixed-event like-sign dimuon mass distribution is normalized to the same-event like-sign combinatorial background distribution in the invariant mass range $2.0-4.5$ GeV/c^2. This factor is then used to normalize the mixed-event unlike-sign dimuon mass distribution.

Figure 2 shows the unlike-sign dimuon spectrum together with the combinatorial background estimated by both methods. Both background distributions from the mixed-event and like-sign methods are consistent, however, the mixed-event background is more statistically stable, because we mix each event with the previous four events. Therefore, the mixed-event background was used to subtract the uncorrelated background from the unlike-sign dimuon spectrum.

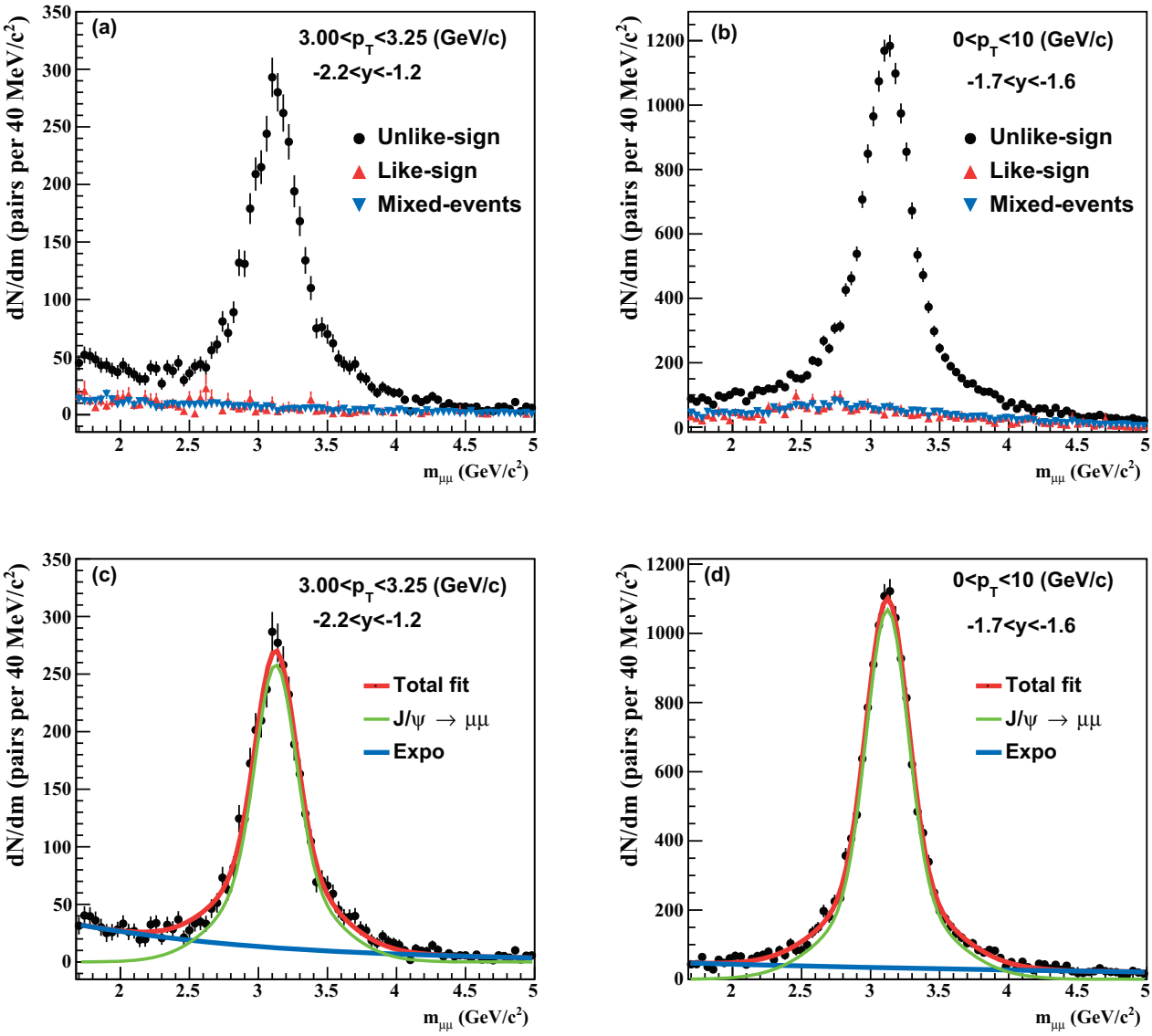

FIG. 2. Raw unlike-sign dimuon spectra (closed [black] circles) along with normalized like-sign background (upward [red] triangles) and normalized mixed-event background (inverted [blue] triangles) for (a) one p_T bin and (b) one rapidity bin. Panels (c) and (d) show the background-subtracted spectra fitted as described in the text for (c) one p_T bin and (d) one rapidity bin.

After subtracting the uncorrelated background, the unlike-sign spectra including the correlated background are fitted by the following function,

$$f(m_{\mu\mu}) = p_0[\frac{(1-p_3)}{\sqrt{2\pi}p_2}\exp(-\frac{1}{2}\frac{(m_{\mu\mu}-p_1)^2}{p_2^2})+ \frac{p_3}{\sqrt{2\pi}p_4}\exp(-\frac{1}{2}\frac{(m_{\mu\mu}-p_1)^2}{p_4^2})]+ p_5\exp(p_6+p_7 m_{\mu\mu}), \quad (1)$$

where $p_0 - p_7$ are free parameters and $m_{\mu\mu}$ is the unlike-sign dimuon mass. The J/ψ shape is better described with two Gaussian distributions, corresponding to the first two terms in Eq. 1, one for the J/ψ peak and a second one with larger width to account for the wider tails, which occurs due to limitations in MuTr resolution, as discussed in sec. II. The peak also includes contribution from $\psi(2S)$, which is not resolved. An exponential is used to describe the continuum contributions from correlated backgrounds. Panels (a) and (b) of Fig. 2 show the raw spectra for selected p_T and rapidity bins and panels (c) and (d) show the spectra after subtracting the combinatorial background fitted with the function described above for those selected bins.

To extract the $\psi(2S)$ signal we improve the mass resolution of the muon tracking systems by utilizing the FVTX. The FVTX being located before the absorber allows measuring the dimuon opening angle before any multiple scattering occurs in the absorber [15]. Using this additional tracking information gives a more precise measurement of the dimuon opening angle and thereby a more precise measurement of the pair mass, as well as rejecting backgrounds from decay muons that emerge from the absorber. However, these additional requirements on the dimuon tracks that are necessary to separate the J/ψ and $\psi(2S)$ peaks also reduce the statistics by a factor of 6 due to the geometric acceptance of FVTX, therefore, we study the dimuon mass spectra in each arm integrated over p_T and rapidity within each arm. The dimuon mass spectrum extracted including the FVTX after subtracting the mixed-event background is shown in Fig. 3.

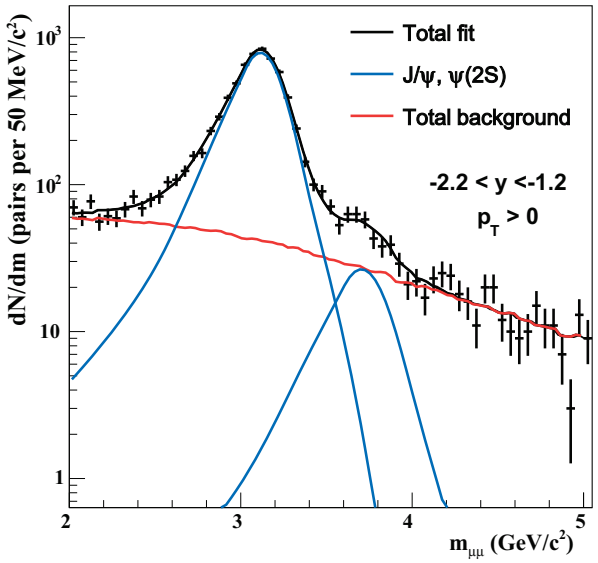

FIG. 3. Raw unlike-sign dimuon spectrum summed over p_T and the whole backward rapidity range, $-2.2 < y < -1.2$.

Given the resolution enhancement, the sum of a Gaussian and a crystal-ball function [16, 17], rather than a double Gaussian, was used for each of J/ψ and $\psi(2S)$ peaks to fit the dimuon mass spectrum. The $\psi(2S)$ peak is expected to be wider than the J/ψ peak, due to the fact that the higher mass and harder p_T spectrum of the $\psi(2S)$ state will produce higher momentum decay muons which have larger uncertainty in their reconstructed momentum in the spectrometer due to a smaller bend in the magnetic field. By selecting only poorly reconstructed tracks, we found a J/ψ width of ≈ 200 MeV/c^2, therefore, the width of the second Gaussian in the fit to the entire sample of tracks is set to 200 MeV/c^2. The ratio of widths of the $\psi(2S)$ to J/ψ is set to 1.15, following expectations of the performance of the muon tracking system [18]. The difference between the centroids of the $\psi(2S)$ and J/ψ peaks is set to the Particle Data Group value of 589 MeV/c^2 [19]. The relative normalization of the second Gaussian is fixed to be the same for both resonances, as are the parameters for the crystal-ball line shape.

B. Detector acceptance and reconstruction efficiency

The acceptance and reconstruction efficiency ($A\varepsilon_{\rm rec}$) of the muon spectrometers, including the MuID trigger efficiency, is determined by running a PYTHIA[1] [20] generated J/ψ signal through a GEANT4-based full detector simulation [21] of PHENIX. The simulation tuned the detector response to a set of characteristics (dead and hot channel maps, gains, noise, etc.) that described the performance of each detector subsystem. The simulated vertex distribution was tuned to match that of the 2013 data. The simulated events are reconstructed in the same manner as the data and the same cuts are applied as in the real data analysis.

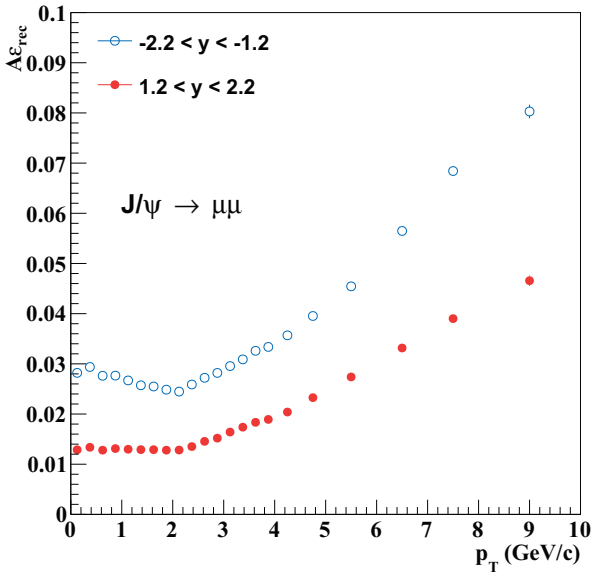

FIG. 4. $A\varepsilon_{\rm rec}$ as a function of p_T for $1.2 < y < 2.2$ (closed [red] circles) and $-2.2 < y < -1.2$ (open [blue] circles).

Figure 4 shows $A\varepsilon_{\rm rec}$ as a function of p_T and rapidity for J/ψ. The relative difference in $A\varepsilon_{\rm rec}$ between the two spectrometers is due to different detection efficiencies of

[1] We used PYTHIA6.421, with parton distribution functions given by CTEQ6LL. The following parameters were modified: MSEL = 0, MSUB(86) = 1, PARP(91) = 2.1, MSTP(51) = 10041, MDME(858,1) = 0, MDME(859,1) = 1, MDME(860,1) = 0, and Tune A.

the MuTr and MuID systems and different amount of absorber material.

In the case of $\psi(2S)$, we are interested in the ratio of its differential cross section to that of J/ψ, therefore, we extract the ratio of $A\varepsilon_{\rm rec}$ for $\psi(2S)$ and J/ψ with addition of the FVTX information in analyzing the simulation to match that of the data analysis. A factor of 0.77 (0.69) is applied to the $\psi(2S)/J/\psi$ ratio extracted from the fit to the invariant mass spectrum to account for differences in acceptance, efficiency, and dimuon trigger efficiencies between the north (south) arm of the muon spectrometer.

C. Differential cross section

The differential cross section is evaluated according to the following relation:

$$\frac{d^2\sigma_\psi}{dydp_T} = \frac{1}{\Delta y \Delta p_T}\frac{N_\psi}{A\varepsilon_{\rm rec} BR}\frac{\sigma_{\rm BBC}}{\varepsilon_{\rm BBC} N_{\rm MB}^{\rm BBC}} \qquad (2)$$

where N_ψ is the extracted J/ψ or $\psi(2S)$ yield in y and p_T bins with Δy and Δp_T widths, respectively. BR is the branching ratio where $BR_{J/\psi\to\mu^+\mu^-} = (5.93 \pm 0.06) \times 10^{-2}$ and $BR_{\psi(2S)\to\mu^+\mu^-} = (7.9\pm0.9)\times10^{-3}$ [19]. $A\varepsilon_{\rm rec}$ is the product of the acceptance and reconstruction efficiency. $N_{\rm MB}^{\rm BBC} = 3.02 \times 10^{12}$ is the number of MB events and $\varepsilon_{\rm BBC} = 0.91 \pm 0.04$ is the efficiency of the MB trigger for events containing a hard scattering [22]. $\sigma_{\rm BBC}$ is the PHENIX BBC cross section, 32.5 ± 3.2 mb at $\sqrt{s} = 510$ GeV, which is determined from the van der Meer scan technique [23].

D. Systematic uncertainties

All systematic uncertainties are evaluated as standard deviations and are summarized in Tables I and II. They are divided into three categories based upon the effect each source has on the measured results:

Type-A: Point-to-point uncorrelated uncertainties allow the data points to move independently with respect to one another and are added in quadrature with statistical uncertainties; however, no systematic uncertainties of this type are associated with this measurement.

Type-B: Point-to-point correlated uncertainties which allow the data points to move coherently within the quoted range to some degree. These systematic uncertainties include a 4% uncertainty from MuID tube efficiency and an 8.2% (2.8%) from MuTr overall efficiency for the north (south) arm. A 3.9% signal extraction uncertainty is assigned to account for the yield variations when using different functions, i.e., second, third and fourth order polynomials, to fit the correlated background and $\approx 3\%$ uncertainty is assigned to account for the $\psi(2S)$ contribution. The systematic uncertainty associated with $A\varepsilon_{\rm rec}$ includes the uncertainty on the input p_T and rapidity distributions which is extracted by varying these distributions over the range of the statistical uncertainty of the data, yielding 4.4% (5.0%) for the north (south) arm. Additional 11.2% (8.8%) systematic effect for the north (south) arm was also considered to account for the azimuthal angle distribution difference between data and simulation. To be consistent with the real data analysis, a trigger emulator was used to match the level-1 dimuon trigger for the data. The efficiency of the trigger emulator was studied by applying it to the data and comparing the resulting mass spectrum to the mass spectrum when applying the level-1 dimuon trigger which resulted in a 1.5% (2%) uncertainty for the north (south) arm. Type-B systematic uncertainties are added in quadrature and amount to 16.0% (12.4%) for the north (south) arm. They are shown as shaded bands on the associated data points.

Type-C: An overall normalization uncertainty of 10% was assigned for the BBC cross section and efficiency uncertainties [24] that allow the data points to move together by a common multiplicative factor.

TABLE I. Systematic uncertainties associated with J/ψ differential cross section calculation in the north (south) arm.

Type-	Origin	north (south)
B	MuID hit efficiency	4.0% (4.0%)
B	MuTr hit efficiency	8.2% (2.8%)
B	Signal extraction	3.9% (3.9%)
B	$\psi(2S)$ contribution	3.0% (3.0%)
B	$A\varepsilon_{\rm rec}$ p_T and y input distributions	4.4% (5.0%)
B	$A\varepsilon_{\rm rec}$ ϕ distribution	11.2% (8.8%)
B	$A\varepsilon_{\rm rec}$ trigger emulator	1.5% (2.0%)
B	Quadratic sum	16.0% (12.4)%
C	MB trigger efficiency	10%

In the measurement of the $\psi(2S)$ to J/ψ ratio, most of the mentioned systematic uncertainties cancel out. However, the fit that was used to extract the yields is more complex and additional systematic uncertainties arose from the constraints applied during the fitting process.

A systematic uncertainty from constraining the normalization factor is determined by varying the mass range over which the factor is calculated and a 3% systematic uncertainty is assigned for both arms. Systematic uncertainty of 3% (7%) was assigned to the north (south) arm on the fit range by varying the range around

the nominal values, 2–5 GeV/c^2. The effect of constraining the second Gaussian peak width to 200 MeV/c^2 was studied by varying the width between 175 and 225 MeV/c^2, resulting in a systematic uncertainty of 12% (10%) in the north (south) arm.

The systematic uncertainty component on $A\varepsilon_{\rm rec}$ that survived the ratio amounts to 2.7% (4.1%) in the north (south) arm. The systematic uncertainties associated with the ratio measurement are summarized in Table II.

TABLE II. Systematic uncertainties associated with the differential cross section ratio of $\psi(2S)$ to J/ψ in the north (south) arm.

Type	Origin	north (south)
B	$\sigma(2s)/\sigma(1s)$ constraint	3% (3%)
B	Background fit mass range	3% (7%)
B	Second Gaussian width constraint	12% (10%)
B	$A\varepsilon_{\rm rec}$	2.7% (4.1%)
B	Quadratic sum	13% (13%)

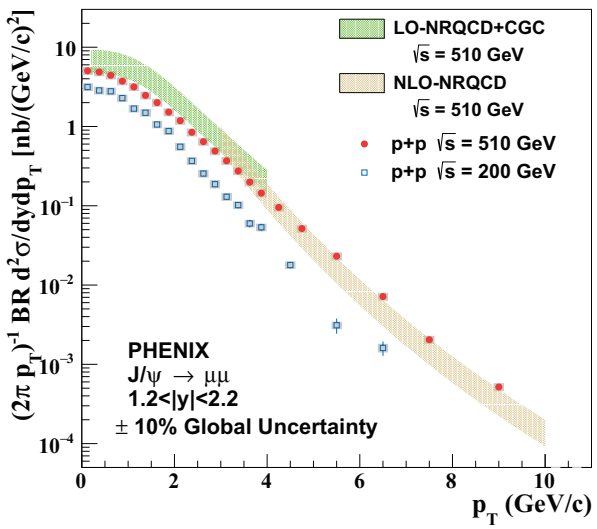

FIG. 5. The inclusive J/ψ differential cross section as a function of p_T at $1.2 < |y| < 2.2$ at 510 GeV (closed [red] circles) and at 200 GeV (open [blue] squares). The error bars represent the statistical uncertainties, and gray shaded bands (although too small to appear on the data points) are added representing the quadratic sum of type-B systematic uncertainties. NRQCD calculations at 510 GeV [8] are also shown.

IV. RESULTS

The inclusive J/ψ differential cross section as a function of p_T is calculated independently for each muon arm, then the results are combined using the best-linear-unbiased-estimate method [25]. Results obtained using the two muon spectrometers are consistent within statistical uncertainties. The combined inclusive J/ψ differential cross section is shown in Fig. 5 and listed in Table III. The gray shaded bands represent the weighted average of the quadratic sum of type-B systematic uncertainties of the north and south arms, $\approx 10.1\%$. The average is weighted based on the statistical uncertainties of each arm.

The data points are corrected to account for the finite width of the analyzed p_T bins [26]. We compare the data to inclusive J/ψ data at 200 GeV [2] which show similar p_T dependence. At low p_T, the data are compared to prompt J/ψ leading-order (LO) NRQCD calculations [8, 13] coupled to a Color Glass Condensate (CGC) description of the low-x gluons in the proton [9]. For the rest of p_T range, the data are compared to prompt J/ψ NLO NRQCD calculations [8, 13]. The LO-NRQCD+CGC calculations overestimate the data at low p_T. The NLO-NRQCD calculations underestimate the data at high p_T, while to some extent, are consistent with the data at intermediate p_T, 3–5 GeV/c. It is important to stress that the nonprompt J/ψ contribution (from excited charmonium states and from B-meson decays) is not included in these calculations. This is expected to be a significant contribution at high p_T; therefore, the addition of the nonprompt J/ψ contribution could account for the difference between the data and calculations [27–29]. The p_T coverage down to zero p_T allows the extraction of the p_T-integrated cross section, BR $d\sigma_{pp}^{J/\psi}/dy(1.2 < |y| < 2.2, 0 < p_T < 10$ GeV/$c) = 54.3 \pm 0.5$ (stat) ± 5.5 (syst) nb.

Inclusive J/ψ differential cross section as a function of rapidity is listed in Table IV and shown in Fig. 6, which also includes PHENIX inclusive J/ψ data at 200 GeV [2] and NLO-NRQCD calculations [8]. The 510 GeV data show a similar rapidity dependence pattern to that of the 200 GeV data. NLO-NRQCD calculations overestimate the data, and this is consistent with what was observed in the case of p_T-dependent differential cross section (see Fig. 5) because the y-dependent differential cross section is dominated by the low-p_T region where NRQCD calculation overestimates the data.

To quantify the feed-down contribution of excited charmonium states, the ratio of the cross section of $\psi(2s)$ to J/ψ, multiplied by their respective branching ratio to dimuons, is measured ($R = 2.84 \pm 0.45\%$) and shown in Fig. 7. This ratio is compared with other p+p and p+A systems at different collision energies [17, 30–38]. The results are consistent with world data within uncertainties with no significant dependence on collision energy.

To better understand the shape of the p_T spectrum for J/ψ at forward rapidity and quantify its hardening at $\sqrt{s}$ = 510 GeV, we calculate the corresponding mean transverse momentum $\langle p_T \rangle$ and mean transverse momentum squared $\langle p_T^2 \rangle$. This is done by fitting the inclusive J/ψ p_T-dependent differential cross sections with the following function [2, 6]:

TABLE III. Differential cross sections in nb/(GeV/c)^2 and p_T in (GeV/c) of inclusive J/ψ with statistical and type-B systematic uncertainties.

$p_T^{\rm min}$	$p_T^{\rm max}$	$\frac{BR}{2\pi p_T}\frac{d^2\sigma}{dydp_T}$
0.00	0.25	$(5.04 \pm 0.23 \pm 0.51) \times 10^{0}$
0.25	0.50	$(4.85 \pm 0.17 \pm 0.49) \times 10^{0}$
0.50	0.75	$(4.42 \pm 0.15 \pm 0.45) \times 10^{0}$
0.75	1.00	$(3.73 \pm 0.13 \pm 0.38) \times 10^{0}$
1.00	1.25	$(3.16 \pm 0.11 \pm 0.32) \times 10^{0}$
1.25	1.50	$(2.47 \pm 0.08 \pm 0.25) \times 10^{0}$
1.50	1.75	$(2.00 \pm 0.07 \pm 0.20) \times 10^{0}$
1.75	2.00	$(1.52 \pm 0.05 \pm 0.15) \times 10^{0}$
2.00	2.25	$(1.18 \pm 0.04 \pm 0.12) \times 10^{0}$
2.25	2.50	$(8.45 \pm 0.30 \pm 0.85) \times 10^{-1}$
2.50	2.75	$(6.44 \pm 0.23 \pm 0.65) \times 10^{-1}$
2.75	3.00	$(4.90 \pm 0.18 \pm 0.50) \times 10^{-1}$
3.00	3.25	$(3.69 \pm 0.14 \pm 0.37) \times 10^{-1}$
3.25	3.50	$(2.74 \pm 0.10 \pm 0.28) \times 10^{-1}$
3.50	3.75	$(1.99 \pm 0.08 \pm 0.20) \times 10^{-1}$
3.75	4.00	$(1.44 \pm 0.06 \pm 0.15) \times 10^{-1}$
4.00	4.50	$(9.53 \pm 0.36 \pm 0.96) \times 10^{-2}$
4.50	5.00	$(5.16 \pm 0.21 \pm 0.52) \times 10^{-2}$
5.00	6.00	$(2.31 \pm 0.09 \pm 0.23) \times 10^{-2}$
6.00	7.00	$(7.17 \pm 0.34 \pm 0.72) \times 10^{-3}$
7.00	8.00	$(2.05 \pm 0.15 \pm 0.21) \times 10^{-3}$
8.00	10.00	$(5.18 \pm 0.44 \pm 0.52) \times 10^{-4}$

TABLE IV. Differential cross sections in nb versus rapidity of inclusive J/ψ over $0 < p_T < 10$ (GeV/c) with statistical and type-B systematic uncertainties.

$y^{\rm min}$	$y^{\rm max}$	$BR\frac{d\sigma}{dy}$ (nb)
-2.20	-2.00	$27.6 \pm 1.3 \pm 4.4$
-2.00	-1.90	$37.7 \pm 1.8 \pm 6.0$
-1.90	-1.80	$47.0 \pm 2.1 \pm 7.5$
-1.80	-1.70	$57.6 \pm 2.6 \pm 9.2$
-1.70	-1.60	$65.2 \pm 2.9 \pm 10.4$
-1.60	-1.50	$71.5 \pm 3.2 \pm 11.4$
-1.50	-1.20	$75.9 \pm 3.4 \pm 12.1$
1.20	1.50	$72.0 \pm 3.4 \pm 11.5$
1.50	1.60	$69.1 \pm 3.2 \pm 11.0$
1.60	1.70	$65.5 \pm 3.0 \pm 10.4$
1.70	1.80	$52.3 \pm 2.4 \pm 8.3$
1.80	1.90	$46.7 \pm 2.2 \pm 7.5$
1.90	2.00	$38.4 \pm 1.9 \pm 6.1$
2.00	2.20	$27.8 \pm 1.4 \pm 4.4$

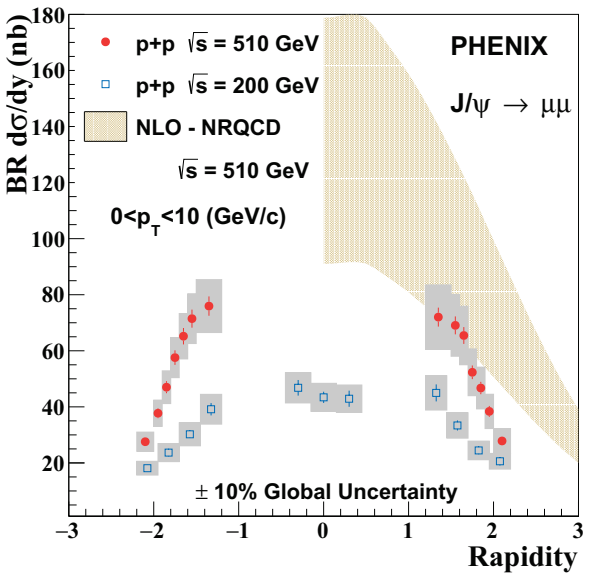

FIG. 6. The inclusive J/ψ differential cross section integrated over $0 < p_T < 10$ GeV/c as a function of rapidity at 510 GeV (closed [red] circles) and at 200 GeV (open [blue] squares). The error bars represent the statistical uncertainties, and the gray shaded band represents the quadratic sum of type-B systematic uncertainties. NLO-NRQCD calculations [8] are also shown.

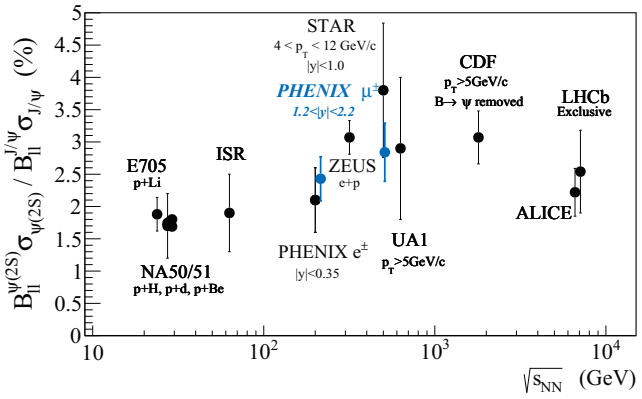

FIG. 7. Comparison of world data on the ratio of $\psi(2s)$ to J/ψ mesons in dilepton decays [7, 17, 30–38]. The associated uncertainties are the quadrature sum of the statistical and systematic uncertainties.

$$f(p_T) = A\frac{p_T}{(1+(\frac{p_T}{B})^2)^n} \qquad (3)$$

where A, B and n are free parameters and their values from the fit are 54.6 ± 0.5, 10.4 ± 0.4 and 0.45 ± 0.06, respectively, and $\langle p_T \rangle$ and $\langle p_T^2 \rangle$ are the first and second moments of Eq. 3 in a given p_T range. This fit results in a $\langle p_T \rangle = 1.90 \pm 0.02 \pm 0.30$ GeV/c and $\langle p_T^2 \rangle = 5.00 \pm 0.06 \pm 0.51$ (GeV/c)^2.

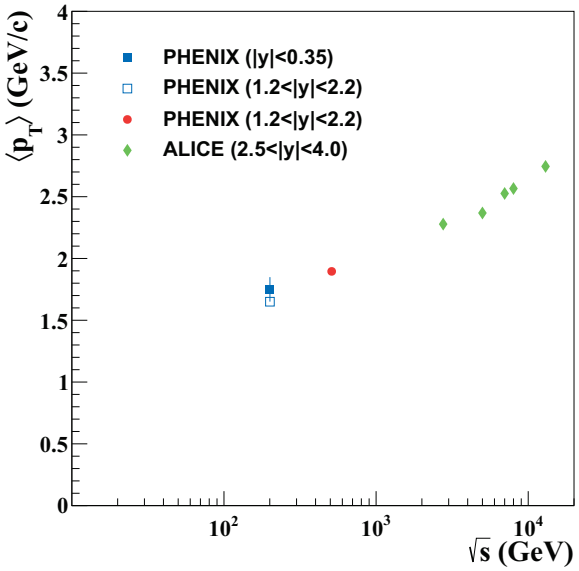

FIG. 8. $\langle p_T \rangle$ as a function of $\sqrt{s}$ for J/ψ from this work at 510 GeV (closed [red] circle), from PHENIX at 200 GeV [2] at midrapidity (closed [blue] square) and forward rapidity (open [blue] square), and from ALICE at different energies [6] (closed [green] diamonds).

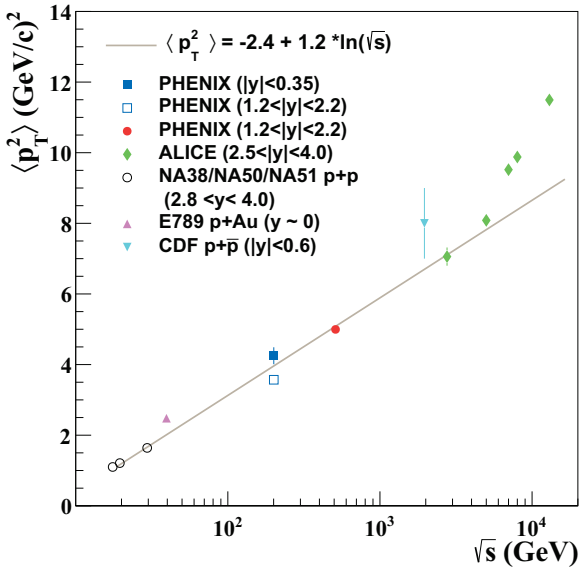

FIG. 9. $\langle p_T^2 \rangle$ as a function of $\sqrt{s}$ for J/ψ. The figure includes results from this work at 510 GeV (closed [red] circle) and PHENIX results at 200 GeV [2] at midrapidity (closed [blue] square) and forward rapidity (open [blue] square). Also shown are higher-energy data from CDF [39] (closed [cyan] downward triangle) and ALICE [6] (closed [green] diamonds). Also shown at lower energies are data from NA38/NA50/NA51 [2, 40] (open [black] circles) and E789 [41] (closed [magenta] upward triangle).

The first error is statistical, and the second is the systematic uncertainty from the maximum shape deviation permitted by the type-B correlated errors.

Figure 8 shows $\langle p_T \rangle$ as a function of $\sqrt{s}$ from this measurement compared with results from 200 GeV PHENIX data at the same rapidity range [2], and results from ALICE at different $\sqrt{s}$ values and in the rapidity range, $2.5 < y < 4.0$ [42]. This result follows the increasing pattern observed between PHENIX results at 200 GeV and ALICE results at 2.76–13 TeV.

Figure 9 shows $\langle p_T^2 \rangle$ as a function of $\sqrt{s}$ from this measurement compared with several other measurements [1, 2, 6, 39, 40, 42, 43]. Similar to $\langle p_T \rangle$, $\langle p_T^2 \rangle$ from this measurement follows the increasing pattern versus $\sqrt{s}$ established by several sets of data over a wide range of energies. Below $\sqrt{s}$ of 2 TeV, the trend is qualitatively consistent with a linear fit of $\langle p_T^2 \rangle$ versus the log of the center of mass energy from Ref. [2]. However, above $\sqrt{s}$ of 2 TeV, the ALICE data indicate $\langle p_T^2 \rangle$ grows at an increased rate which is interpreted by authors of Ref. [6] as due to the fact that ALICE data sets have different p_T ranges. The bottom cross section also increases with increasing $\sqrt{s}$, changing the relative prompt and B-meson decay contributions to the inclusive J/ψ samples discussed here [27, 44]. This may also contribute to the observed differences in the measured $\langle p_T^2 \rangle$.

The $d\sigma_{pp}^{J/\psi}/dy$ measurement at $\sqrt{s} = 510$ GeV offers an opportunity to test the center-of-mass energy dependence of the p_T-integrated cross section. Moreover, it bridges the gap between RHIC data at 200 GeV and ALICE data starting at 2.76 TeV [3–6]. However, ALICE data are collected at mid ($|y| < 0.9$) and forward ($2.5 < y < 4.0$) rapidities and to have a proper comparison we interpolate the ALICE data to the PHENIX forward rapidity range, $1.2 < y < 2.2$. This is done by fitting the PYTHIA generated $d\sigma/dy$ distribution at each energy to the data at the same energy with only the normalization as a free parameter. An example is shown in Fig. 10. We used several PYTHIA [45] tunes including PHENIX default, tune-A, modified tune-A and ATLAS-CSC [46]. After fitting each of these PYTHIA tunes to the data, we extracted $d\sigma/dy$ at $1.2 < y < 2.2$, from these fits. The rms value of the extracted $d\sigma/dy$ from the different fits is used in the comparison to RHIC data. The error on the rms value is the rms of the errors associated with the fit results.

Figure 11 shows the results from this measurement, 200 GeV PHENIX data (closed [blue] squares), ALICE data (open [green] circles), and interpolated ALICE data (closed [red] circles) at several energies. Figure 11 shows that the data are well described by a power law, $d\sigma_{pp}^{J/\psi}/dy \propto (\sqrt{s})^b$, where the exponent is $b = 0.72 \pm 0.03$.

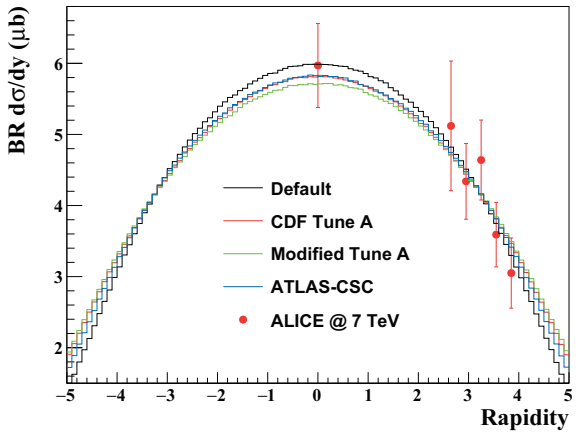

FIG. 10. Inclusive J/ψ differential cross section as a function of rapidity at $\sqrt{s} = 7$ TeV [3] fitted with different PYTHIA tunes at the same energy.

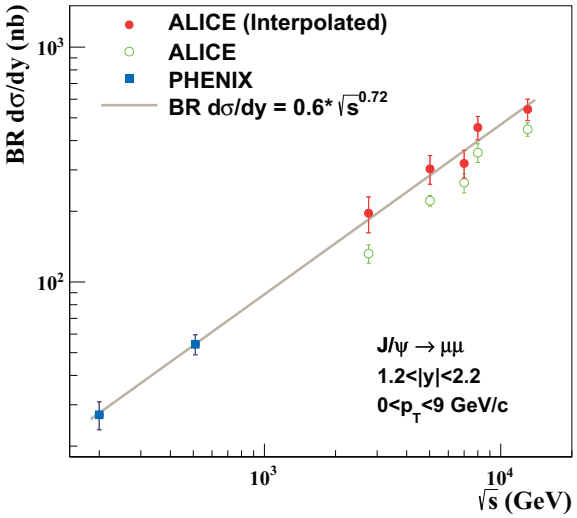

FIG. 11. Inclusive J/ψ differential cross section, $d\sigma/dy$, as a function of $\sqrt{s}$. The vertical errors correspond to the quadratic sum of the statistical and type-B systematic uncertainties.

V. SUMMARY

We studied inclusive J/ψ production in p+p collisions at $\sqrt{s} = 510$ GeV for $1.2 < |y| < 2.2$ and $0 < p_T < 10$ GeV/c, through the dimuon decay channel. We measured inclusive J/ψ differential cross sections as a function of p_T as well as a function of rapidity. The p_T integrated differential cross section multiplied by J/ψ branching ratio to dimuons is $BR\ d\sigma_{pp}^{J/\psi}/dy$ $(1.2 < |y| < 2.2, 0 < p_T < 10$ GeV/$c) = 54.3 \pm 0.5$ (stat) $\pm$ 5.5 (syst) nb. With these data measured over a wide p_T range, we calculated $\langle p_T \rangle$, $\langle p_T^2 \rangle$ and $d\sigma/dy$. The results were compared to similar quantities at different energies from RHIC and LHC to study their $\sqrt{s}$ dependence. These new measurements could put stringent constraints on J/ψ production models.

The inclusive J/ψ differential cross sections were compared to prompt J/ψ calculations. These calculations included LO-NRQCD+CGC at low p_T and NLO-NRQCD for the rest of p_T range. These model calculations overestimated the data at low p_T and underestimated the data at high p_T. The nonprompt J/ψ contribution was not included which could account for the underestimation at high p_T where the nonprompt processes are significant.

In addition, we measured the ratio of the cross section of $\psi(2s)$ to J/ψ, multiplied by their respective branching ratio to dimuons, $R = 2.84 \pm 0.45\%$. The result is consistent with world data within uncertainties with no dependence on collision energy.

ACKNOWLEDGMENTS

We thank the staff of the Collider-Accelerator and Physics Departments at Brookhaven National Laboratory and the staff of the other PHENIX participating institutions for their vital contributions. We acknowledge support from the Office of Nuclear Physics in the Office of Science of the Department of Energy, the National Science Foundation, Abilene Christian University Research Council, Research Foundation of SUNY, and Dean of the College of Arts and Sciences, Vanderbilt University (U.S.A), Ministry of Education, Culture, Sports, Science, and Technology and the Japan Society for the Promotion of Science (Japan), Conselho Nacional de Desenvolvimento Científico e Tecnológico and Fundação de Amparo à Pesquisa do Estado de São Paulo (Brazil), Natural Science Foundation of China (People's Republic of China), Croatian Science Foundation and Ministry of Science and Education (Croatia), Ministry of Education, Youth and Sports (Czech Republic), Centre National de la Recherche Scientifique, Commissariat à l'Énergie Atomique, and Institut National de Physique Nucléaire et de Physique des Particules (France), Bundesministerium für Bildung und Forschung, Deutscher Akademischer Austausch Dienst, and Alexander von Humboldt Stiftung (Germany), J. Bolyai Research Scholarship, EFOP, the New National Excellence Program (ÚNKP), NKFIH, and OTKA (Hungary), Department of Atomic Energy and Department of Science and Technology (India), Israel Science Foundation (Israel), Basic Science Research and SRC(CENuM) Programs through NRF funded by the Ministry of Education and the Ministry of Science and ICT (Korea). Physics Department, Lahore University

of Management Sciences (Pakistan), Ministry of Education and Science, Russian Academy of Sciences, Federal Agency of Atomic Energy (Russia), VR and Wallenberg Foundation (Sweden), the U.S. Civilian Research and Development Foundation for the Independent States of the Former Soviet Union, the Hungarian American Enterprise Scholarship Fund, the US-Hungarian Fulbright Foundation, and the US-Israel Binational Science Foundation.

[1] F. Abe *et al.* (CDF Collaboration), "Inclusive J/ψ, $\psi(2S)$ and b quark production in $\bar{p}p$ collisions at $\sqrt{s} = 1.8$ TeV," Phys. Rev. Lett. **69**, 3704 (1992).

[2] A. Adare *et al.* (PHENIX Collaboration), "J/ψ Production versus Transverse Momentum and Rapidity in $p+p$ Collisions at $\sqrt{s} = 200$ GeV," Phys. Rev. Lett. **98**, 232002 (2007).

[3] K. Aamodt *et al.*, "Rapidity and transverse momentum dependence of inclusive J/ψ production in pp collisions at $\sqrt{s} = 7$ TeV," Phys, Lett. B **704**, 442 (2011).

[4] B. Abelev *et al.*, "Inclusive J/ψ production in pp collisions at $\sqrt{s}$=2.76 TeV," Phys. Lett. B **718**, 295 (2012).

[5] J. Adam *et al.*, "Inclusive quarkonium production at forward rapidity in pp collisions at $\sqrt{s}$=8 TeV," Eur. Phys. J. C **76**, 184 (2016).

[6] S. Acharya *et al.*, "Energy dependence of forward-rapidity J/ψ and $\psi(2S)$ production in pp collisions at the LHC," Eur. Phys. J. C **77**, 392 (2017).

[7] J. Adam *et al.* (STAR Collaboration), "Measurements of the transverse-momentum-dependent cross sections of J/ψ production at mid-rapidity in proton + proton collisions at $\sqrt{s} = 510$ and 500 GeV with the STAR detector," Phys. Rev. D **100**, 052009 (2019).

[8] Y.-Q. Ma, K. Wang, and K.-T. Chao, "$J/\psi(\psi')$ Production at the Tevatron and LHC at $\mathcal{O}(\alpha_s^4 v^4)$ in Nonrelativistic QCD ," Phys. Rev. Lett. **106**, 042002 (2011).

[9] Y.-Q. Ma and R. Venugopalan, "Comprehensive Description of J/ψ Production in Proton-Proton Collisions at Collider Energies," Phys. Rev. Lett. **113**, 192301 (2014).

[10] H. Fritzsch, "Producing heavy quark flavors in hadronic collisions' A test of quantum chromodynamics," Phys. Lett. B **67**, 217 (1977).

[11] J.F. Amundson, O.J.P. *É*boli, E.M. Gregores, and F. Halzen, "Quantitative tests of color evaporation: charmonium production," Phys. Lett. B **390**, 323 (1997).

[12] R. Baier and R. Rückl, "Hadronic production of J/ψ and γ: Transverse momentum distributions," Phys. Lett. B **102**, 364 (1981).

[13] G. T. Bodwin, E. Braaten, and G. P. Lepage, "Rigorous QCD analysis of inclusive annihilation and production of heavy quarkonium," Phys. Rev. D **51**, 1125 (1995).

[14] K. Adcox *et al.* (PHENIX Collaboration), "PHENIX detector overview," Nucl. Instrum. Methods Phys. Res., Sec. A **499**, 469–479 (2003).

[15] C. Aidala *et al.*, "The PHENIX Forward Silicon Vertex Detector," Nucl. Instrum. Methods Phys. Res., Sec. A **755**, 44 (2014).

[16] J. Gaiser, *Charmonium Spectroscopy From Radiative Decays of the J/ψ and ψ'*, Ph.D. dissertation., Stanford Linear Accelerator Center, Stanford University, Stanford, California 94305 (1983), SLAC Stanford - SLAC-255 (82,REC.JUN.83).

[17] A. Adare *et al.* (PHENIX Collaboration), "Measurement of the relative yields of $\psi(2S)$ to $\psi(1S)$ mesons produced at forward and backward rapidity in $p+p$, $p+$Al, $p+$Au, and ^{3}He+Au collisions at $\sqrt{s_{NN}} = 200$ GeV," Phys. Rev. C **95**, 034904 (2017).

[18] H. Akikawa *et al.*, "PHENIX Muon Arms," Nucl. Instrum. Methods Phys. Res., Sec. A **499**, 537 (2003).

[19] K.A. Olive *et al.* (Particle Data Group), "Review of Particle Physics," Chin. Phys. C **38**, 090001 (2014).

[20] T. Sjö*s*trand *et al.*, "High-energy-physics event generation with PYTHIA6.1," Comput. Phys. Commun. **135**, 238 (2001).

[21] S. Agostinelli *et al.* (GEANT4 Collaboration), "GEANT4: A simulation toolkit," Nucl. Instrum. Methods Phys. Res., Sec. A **506**, 250 (2003).

[22] A. Adare *et al.* (PHENIX Collaboration), "Inclusive cross section and double-helicity asymmetry for π^0 production at midrapidity in $p+p$ collisions at $\sqrt{s} = 510$ gev," Phys. Rev. D **93**, 011501 (2016).

[23] A. Adare *et al.* (PHENIX Collaboration), "Cross Section and Parity Violating Spin Asymmetries of $W^{\pm}$ Boson Production in Polarized $p+p$ Collisions at $\sqrt{s} = 500$ GeV," Phys. Rev. Lett. **106**, 062001 (2011).

[24] S. S. Adler *et al.* (PHENIX Collaboration), "Midrapidity Neutral-Pion Production in Proton-Proton Collisions at $\sqrt{s} = 200$ GeV," Phys. Rev. Lett. **91**, 241803 (2003).

[25] R. Nisius, "On the combination of correlated estimates of a physics observable," Eur. Phys. J. C **74**, 3004 (2014).

[26] G. D. Lafferty and T. R. Wyatt, "Where to stick your data points: The treatment of measurements within wide bins," Nucl. Instrum. Methods Phys. Res., Sec. A **355**, 541 (1995).

[27] C. Aidala *et al.* (PHENIX Collaboration), "Measurements of $B \to J/\psi$ at forward rapidity in $p+p$ collisions at $\sqrt{s} = 510$ GeV," Phys. Rev. D **95**, 092002 (2017).

[28] M. Cacciari, P. Nason, and R. Vogt, "QCD Predictions for Charm and Bottom Quark Production at RHIC," Phys. Rev. Lett. **95**, 122001 (2005).

[29] R. E. Nelson, R. Vogt, and A. D. Frawley, "Narrowing the uncertainty on the total charm cross section and its effect on the J/ψ cross section," Phys. Rev. C **87**, 014908 (2013).

[30] B. Alessandro *et al.*, "J/ψ and ψ' production and their normal nuclear absorption in proton-nucleus collisions at 400 GeV," Eur. Phys. J. C **48**, 329 (2006).

[31] A. Adare *et al.* (PHENIX Collaboration), "Ground and excited state charmonium production in $p+p$ collisions at $\sqrt{s}$ =200 GeV," Phys. Rev. D **85**, 092004 (2012).

[32] L. Antoniazzi *et al.*, "Production of J/ψ via ψ' and χ decay in 300 GeV/c proton- and $\pi^{\pm}$-nucleon interactions," Phys. Rev. Lett. **70**, 383 (1993).

[33] M. C. Abreu *et al.*, "J/ψ, ψ(2S) and Drell-Yan production in pp and pd interactions at 450 GeV/c," Phys. Lett. B **438**, 35 (1998).

[34] A. G. Clark *et al.*, "Electron pair production at the CERN ISR," Nucl. Phys. B **142**, 29 (1978).

[35] C. Albajar *et al.*, "J/ψ and ψ' production at the CERN $p\bar{p}$ collider," Phys. Lett. B **256**, 112 (1991).

[36] F. Abe *et al.* (CDF Collaboration), "J/ψ and ψ' Production in $p\bar{p}$ Collisions at $\sqrt{s} = 1.8$ TeV," Phys. Rev. Lett. **79**, 572 (1997).

[37] R. Aaij *et al.*, "Exclusive J/ψ and $\psi(2S)$ production in pp collisions at $\sqrt{s} = 7$ TeV," J. Phys. G **40**, 045001 (2013).

[38] B. Abelev *et al.* (ALICE Collaboration), "Measurement of quarkonium production at forward rapidity in pp collisions at $\sqrt{s} = 7$ TeV," Eur. Phys. J. C **74**, 2974 (2014).

[39] D. Acosta *et al.* (CDF Collaboration), "Measurement of the J/ψ meson and b-hadron production cross sections in $p\bar{p}$ collisions at $\sqrt{s} = 1960$ GeV," Phys. Rev. D **71**, 032001 (2005).

[40] O. Drapier, *Study of the transverse momentum distributions of dimuons produced in nucleus-nucleus collisions at the CERN SPS*, Thèse d'habilitation thesis, Université Claude Bernard-Lyon (1998).

[41] M. H. Schub *et al.*, "Measurement of J/ψ and ψ' production in 800 GeV/c proton-gold collisions," Phys. Rev. D **52**, 1307 (1995).

[42] R. Aaij, "Measurement of $\psi(2S)$ polarization in pp collisions at $\sqrt{s} = 7$ TeV," Eur. Phys. J. C **74**, 2872 (2014).

[43] D. Acosta *et al.* (CDF Collaboration), "Cross section for forward J/ψ production in $p\bar{p}$ collisions at $\sqrt{s} = 1.8$ TeV," Phys. Rev. D **66**, 092001 (2002).

[44] B. Abelev *et al.* (ALICE Collaboration), "Measurement of prompt J/ψ and beauty hadron production cross sections at midrapidity in pp collisions at $\sqrt{s} = 7$ TeV," (2012), J. High Energy Phys. **11 (2012)** 065.

[45] T. Sjöstrand, S. Mrenna, and P. Skands, "PYTHIA6.4 physics and manual," (2006), J. High Energy Phys. **05 (2006)** 026.

[46] T. Sjöstrand and P. Z. Skands, "Transverse-momentum-ordered showers and interleaved multiple interactions," Eur. Phys. J. C **39**, 129 (2005).